

Persisting of Polar Distortion with Electron Doping in Lone-Pair Driven Ferroelectrics

Xu He¹ and Kui-juan Jin^{1,2,*}

¹*Beijing National Laboratory for Condensed Matter Physics,
Institute of Physics, Chinese Academy of Sciences, Beijing 100190, China*
²*Collaborative Innovation Center of Quantum Matter, Beijing 100190, China*

Free electrons can screen out long-range Coulomb interaction and destroy the polar distortion in some ferroelectric materials, whereas the coexistence of polar distortion and metallicity were found in several non-central-symmetric metals (NCSMs). Therefore, the mechanisms and designing of NCSMs have attracted great interests. In this work, by first-principles calculation, we found the polar distortion in the lone-pair driven ferroelectric material PbTiO_3 can not only persist, but also increase with electron doping. We further analyzed the mechanisms of the persisting of the polar distortion. We found that the Ti site polar instability is suppressed but the Pb site polar instability is intact with the electron doping. The Pb-site instability is due to the lone-pair mechanism which can be viewed as a pseudo-Jahn-Teller effect, a mix of the ground state and the excited state by ion displacement from the central symmetric position. The lone-pair mechanism is not strongly affected by the electron doping because neither the ground state nor the excited state involved is at the Fermi energy. The enhancement of the polar distortion is related to the increasing of the Ti ion size by doping. These results show that the long-pair stereoactive ions can be used for designing NCSMs.

PACS numbers: 77.80.-e, 77.84.Bw, 71.20.-b

I. INTRODUCTION

In ferroelectric materials, there is a delicate balance between the short-range repulsion which favors the non-polar structure and the long-range Coulomb interaction which favors the ferroelectric state^{1,2}. Free carriers screen out the long-range Coulomb interaction, thus it can reduce the polar distortion. For example, in a prototypical ferroelectric material BaTiO_3 , the ferroelectric distortion is weakened with electron doping, and eventually disappears when a critical concentration is reached³⁻⁶. The screening of the Coulomb interaction was believed to be the reason for the weakening or disappearing of the polar distortion for BaTiO_3 ^{5,6}. Although the screening effect of the carriers can also inhibit the polar distortion in many other ferroelectric materials, there are exceptions which have attracted a lot of attentions and efforts. Anderson and Blount pointed out that while free electrons can screen out the electric field, the transverse optical soft phonons can lead to polar distortion⁷. A few “ferroelectric” metals, or more precisely non-central-symmetric metals (NCSMs) have been found or proposed, such as perovskite structure LiOsO_3 ⁸⁻¹², MgReO_3 ¹⁰, and the cation-ordered $\text{SrCaRu}_2\text{O}_6$ ¹³. The possible mechanisms of the NCSMs have been discussed by several authors. Xiang suggested that the long-range Coulomb interaction is not necessary for the polar distortion; the short-range pair interactions, which are not screened out by free electrons, can drive the polar distortion¹⁰. Puggioni and Rondinelli proposed that the non-centrosymmetric structure can exist if the coupling of the soft phonon mode and the electrons at the Fermi level is weak¹³. Benedek and Birol proposed that polar distortion can emerge through a geometric mechanism in metals¹⁴.

Although the NCSM structures are no longer suitable for the usage as ferroelectric materials because of the metallicity, other interesting properties are found in NCSMs, like the unconventional optical responses^{15,16}, magnetoelectricity¹⁷, superconductivity¹⁸, and thermoelectricity¹³. A deeper understanding of the mechanisms of NCSM could help finding new NCSMs. The purpose of this work is to seek a possible mechanism of NCSMs so new NCSMs can be found or designed.

In this work, by studying the polar distortion in electron-doped PbTiO_3 , we show that the lone-pair driven polar distortion is compatible with metallicity. The lone pair mechanism for the polar distortion in non-doped PbTiO_3 has been long studied¹⁹⁻²². In PbTiO_3 , the hybridization between the Pb (6s, 6p) bands and O 2p bands reduces the short-range repulsion, resulting in a large polar distortion, which is often referred as lone-pair driven ferroelectricity. The lone-pair driven ferroelectricity can be interpreted as the result of the Pseudo-Jahn-Teller effect (PJTE)²³⁻²⁶ which is local. Therefore, it is possible that the lone pair mechanism can still drive the polar distortion even if the long-range interaction is screened. We found that the polar distortion in PbTiO_3 not only persists but also is enhanced with the electron doping. Then by analyzing the evolution of the phonon and the force constant matrices (FCM's), we found that the A-site instability, which is caused by the lone-pair mechanism, is responsible for the persisting of the polar distortion, because the electronic states involved are far away from the Fermi energy. We showed that enhancement of the polar distortion is related to the increasing of the Pb-O distance. We discussed the generalizability of the results from PbTiO_3 to other lone-pair driven ferroelectric materials and propose that the lone-pair stereoactive ions can be used for the designing of NCSMs.

* Correspondence and requests for materials should be addressed to Kui-juan Jin. Email: kjjin@iphy.ac.cn

II. METHODS

The density functional theory (DFT) calculations were carried out by using the projected augmented wave (PAW)²⁷ pseudopotentials as implemented in the Vienna *ab initio* simulation package (VASP)²⁸. The energy cutoff of the plane wave basis set was 500 eV. The exchange-correlation functional with local density approximation (LDA) as parameterized by Perdew and Zunger (PZ)²⁹ was used. The reference electronic configurations for the pseudopotentials are Pb $5d^{10}6s^26p^2$, Ba $5s^25p^66s^2$, Ti $3s^23p^63d^4$, and O $2s^22p^6$, respectively. An $8 \times 8 \times 8$ Γ -centered k -point mesh was used to represent the reciprocal space. The calculated $P4mm$ structure has a tetragonality (c/a) of 1.04 and a volume of 60.2 \AA^3 , agreeing well with the experimental data and previous DFT calculations^{30,31}.

Electron doping is added into the structure with additional neutralizing background charges, instead of dopants like oxygen vacancies. In this case, however, the energy converges very slowly with respect to the size of the supercell. The problem is solved by adding a first order correction (image charge correction) to the total energy. The phonon frequencies and the FCM's were calculated using the density functional perturbation theory³² (DFPT) method as implemented in VASP and the phonopy³³ package. The non-analytic contribution (NAC)³⁴ to the phonon and FCMs³⁵ was not considered. The Born effective charges (BEC's) for structures with free charges are not well defined, inhibiting the calculation of the NAC. The NAC only affects the longitudinal optical (LO) phonon frequencies, whereas the polar distortion is caused by the transverse optical (TO) phonon. We also checked the phonon results with NAC added against others' work³⁶ and the results agree well. The comparisons of BEC's and the Γ -point phonon frequencies for the $Pm\bar{3}m$ structure are in table I and table II, respectively. The Γ point FCMs were calculated in a $1 \times 1 \times 1$ $Pm\bar{3}m$ structure. A $2 \times 2 \times 2$ supercell of 40 atoms was used for the phonon band calculation.³⁷ The phonon frequencies were calculated with the structures fully relaxed. A Γ -centered $20 \times 20 \times 20$ Monkhorst-Pack grid was used to calculate the phonon density of states (PDOS). The crystal orbital hamilton population^{38,39} (COHP) analyses were carried out with the LOBSTER⁴⁰ code. The crystal structures and the contour maps of the electron localization functions⁴¹ (ELFs) were visualized using the VESTA package⁴².

The ferroelectric polarization in a structure with free charges is not well defined. Therefore, the structural polar distortion is discussed instead of the ferroelectric polarization in the present work.

III. RESULTS AND DISCUSSION

Here we show the enhancement of the polar distortion with electron doping in $PbTiO_3$. The ferroelectric $PbTiO_3$ structure with $P4mm$ symmetry group is shown in Fig. 1, where the Pb and Ti cations displace along the c direction, and the O anions displace in the opposite direction. The change of the polar distortion in $P4mm$ $PbTiO_3$ structure with the concentration of the doped carriers (n_e) is shown in Fig. 2 (a). As n_e increases,

the tetragonality (c/a) of the lattice and the relative displacements of the Pb and Ti cations from the O anions increase. These phenomena show the enhancement of the polar distortion, in contrast to what happens in the $P4mm$ $BaTiO_3$ ³⁻⁶, where the tetragonality and the cation-anion relative displacements both decrease to zero when the electron doping level is about 0.1 $e/u.c.$, as shown in Fig. 2 (b). The polar distortion can be decomposed into three Γ -point normal modes⁴³ (Fig. 2), namely the Slater, Last, and Axe modes. The Slater mode⁴⁴ (Fig. 2 (c)) involves the displacement of the Ti ion from the center of the oxygen octahedron, which is corresponding to the Ti-site instability. The Last mode⁴⁵ (Fig. 2 (d)) involves the displacement of the A-site ions against the TiO_6 octahedron, which is corresponding to the A-site instability. The Axe mode⁴⁶ (Fig. 2 (e)) involves the relative displacement of the O1 and O2 ions, which is corresponding to the distortion of the oxygen octahedron. It can be seen that in $PbTiO_3$, both Slater mode and Last mode contribute to the polar distortion. The amplitudes of them both increase as electrons are doped. For $BaTiO_3$, Slater mode is predominant and decreases with electron doping. The difference implies that the Pb-site instability may drive the enhancement of the polar distortion in $PbTiO_3$.

We also found that the lattice volumes increase with n_e in both $PbTiO_3$ and $BaTiO_3$ (Fig. 2).

In our calculation, the doping level ranges from 0 to about 0.4 $e/u.c.$. Such high doping level is hard or even impossible to be realized by adding dopants such as oxygen vacancies to the structure without changing the structural properties dramatically. Therefore, the results for high-doping levels presented here may not be applicable directly. However, it is still beneficial to see what happens in the hypothetical heavily doped structure in which the long-range Coulomb interaction should be mostly screened out.

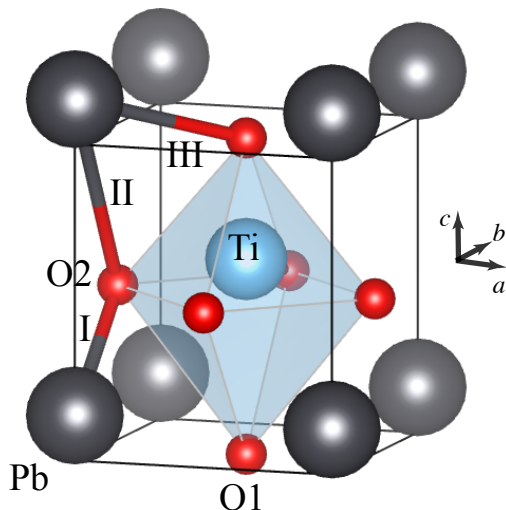


FIG. 1: The structure of $P4mm$ $PbTiO_3$. The black, blue, and red spheres are the Pb, Ti, and O ions, respectively. O1 and O2 are the in-plane and apical oxygen ions, respectively. Due to the displacements of the ions in the c direction, there are two kinds of Pb-O2 bonds, the shorter one (type I) and the longer one (type II). The Pb-O1 bonds are labeled as type III.

In BaTiO₃, the decreasing of the polar distortion with electron doping was believed to be because of the screening effect^{5,6}. The doped electrons screen out the long-range Coulomb interaction. The screening length λ can be estimated with the Thomas-Fermi model $\lambda = \sqrt{\varepsilon/e^2 D(E_F)}$, where ε is the dielectric permittivity, and $D(E_F)$ is the density of states (DOS) at the Fermi level. As the concentration of doped electrons increases, the DOS at the Fermi energy increases, and thus the screening length decreases. The values of ε and the values of $D(E_F)$ for PbTiO₃ are close to those for BaTiO₃, respectively. ($\varepsilon(\text{PbTiO}_3)$ and $\varepsilon(\text{BaTiO}_3)$ are $81\varepsilon_0$ and $78\varepsilon_0$ from the LDA and DFPT⁴⁷ calculation⁴⁸, respectively. When the concentration of electrons is 0.2 e/u.c., the $D(E_F)$ are 0.7 and 1.1 states/(eV·u.c.), and consequently the screening length are about 5 Å and 6 Å in PbTiO₃ and BaTiO₃, respectively.) Therefore, the screening effects of the long-range Coulomb interaction are comparable in these two materials. The polar distortion is gradually destroyed by the screening effect in BaTiO₃. Then what is the intrinsic reason for the opposite trend of the polar distortion with doped electrons in PbTiO₃ from that in BaTiO₃?

	Z_{Pb}^*	Z_{Ti}^*	$Z_{\text{O1},xx}^*$	$Z_{\text{O1},zz}^*$
this work	3.92	7.25	-2.62	-5.94
Ref. 36	3.90	7.06	-2.56	-5.83

TABLE I: Born effective charge of PbTiO₃ in cubic structure. The unit is $|e|$. Only the xx , yy , and zz part of the BEC tensors are non-zero. For Pb and Ti, $Z_{xx}^* = Z_{yy}^* = Z_{zz}^*$. For O, $Z_{\text{O1},yy}^* = Z_{\text{O1},xx}^* = Z_{\text{O2},yy}^* = Z_{\text{O2},zz}^*$, $Z_{\text{O2},xx}^* = Z_{\text{O1},zz}^*$. The results in Ref. 36 were calculated with LDA.

Aside from the long-range Coulomb interaction, the covalence between Ti and O causes the Ti-site polar instability in both BaTiO₃ and PbTiO₃. The difference is that the covalence between Pb-O also causes the Pb-site polar instability. Bersuker *et al.* interpreted both the Ti-site and Pb-site instabilities as the results of PJTE^{23,24}. To see which site is responsible for the polar distortion and how the polar instabilities are affected by the electron doping, we consider the evolution of the phonon modes in the paraelectric $Pm\bar{3}m$ phase with the electron doping. The transition to a ferroelectric phase from a paraelectric phase is featured with imaginary phonon frequencies in the paraelectric phase. The phonon bands of $Pm\bar{3}m$ phase were calculated, as shown in Fig. 3. Without electron doping, the imaginary frequencies are at Γ , R , and M in the $Pm\bar{3}m$ phase, as shown in Fig. 3 (a). With electrons doped, the imaginary frequency at Γ point (Fig. 3 (b)) corresponding to the ferroelectric distortion firstly decreases and then in-

	TO1	TO2	TO3	LO1	LO2	LO3
This work	3.84i	3.90	15.32	3.15	12.40	20.96
Ref. 36	4.32i	3.63	14.90	3.12	12.30	20.18

TABLE II: Γ -point phonon frequencies of PbTiO₃ in cubic structure with NAC added. The unit is THz. The results in Ref. 36 were calculated with LDA/DFPT.

creases, as shown in Fig. 3 (g), unlike that in BaTiO₃⁵, where the imaginary frequencies disappear as the concentration of electrons increases. The atom projected phonon densities of states (PDOS) for $n_e=0$ and $n_e=0.2$ e/u.c. are shown in Fig. 3 (c) and (d), respectively. For both $n_e=0$ and $n_e=0.2$ e/u.c., most of the PDOS in the imaginary frequency region is projected on the Pb sites, and a small portion is projected on the apical Oxygen site O2, indicating that the soft phonons are from the Pb atoms and the O atoms in the side plane. The results consist with that the lone -pair is from the Pb-O electron hybridization⁴⁹.

We also checked the phonon bands of the $P4mm$ phase with and without electron doping, and we found that there are no imaginary frequencies in the phonon bands in the $P4mm$ phase (Fig. 3 (e and f)), indicating that the $P4mm$ phase are stable.

To further investigate the change of the lattice ferroelectric instabilities, we calculated the Γ point FCM's⁵⁰ (FCMs) of the PbTiO₃ and BaTiO₃ cubic structures with various concentration of doped electrons. The elements of the FCM $D_{ij}^{xy} = \partial^2 E / \partial u_i \partial u_j$ is the derivative of the energy with the displacements of two atoms u_i and u_j , where u_i is along x direction and u_j is along the y direction. Due to the $Pm\bar{3}m$ symmetry, only the xx , yy , and zz components are none zero. For the same i and j pair, the xx , yy , and zz components are equal to each other. So we only have to discuss the zz components here, i.e., the displacements are all along the z direction. Thus we omit the superscript of D_{ij}^{xy} . The changes of the FCMs are shown in Fig. 4.

For j equals to i , the element $\partial^2 E / \partial u_i^2$, which is the second derivative of the energy with the position of the atom, is known as self-force constants. A positive (negative) value of the self-force constant for an atom indicates an increasing (decreasing) of the energy by solely displacing that atom in the supercell with other atoms frozen. The self-force constants of PbTiO₃ and BaTiO₃ are shown in Figs. 4 (a) and (b), respectively. In both PbTiO₃ and BaTiO₃, the self-force constants of Ti increase as n_e increases, which means that if the Ti atoms are displaced from their central symmetry positions, the energy costs would be higher, which reduces the Ti-site instability. In PbTiO₃, the self-force constant of Pb, which is the smallest among all self-force constants, decrease with n_e and eventually get below zero, meaning that the tendency of Pb ions displacing from the central symmetry positions increases. In BaTiO₃, though the self-force constant of Ba ion also decreases with n_e , it is still much larger than zero, which stabilizes the Ba ion at the central symmetry position.

Then we look into the interatomic FCs (IFC's). The IFC's of PbTiO₃ and BaTiO₃ are shown in Figs. 4 (d) and (e), respectively. A positive D_{ij} means that the energy would be lowered if the displacements of the two atoms labeled as i and j are along the different direction. It must be noted that an IFC is not corresponding to an individual bond but to the sum of all the interaction between two atoms, which may involve several bonds in a unit cell due to the periodic boundary condition. For example, if we consider only the nearest neighbor interaction, the Pb-O2 IFC is corresponding to the bonds of a Pb ion with all the eight nearest O2 ions, involving 4 type I Pb-O2 bonds

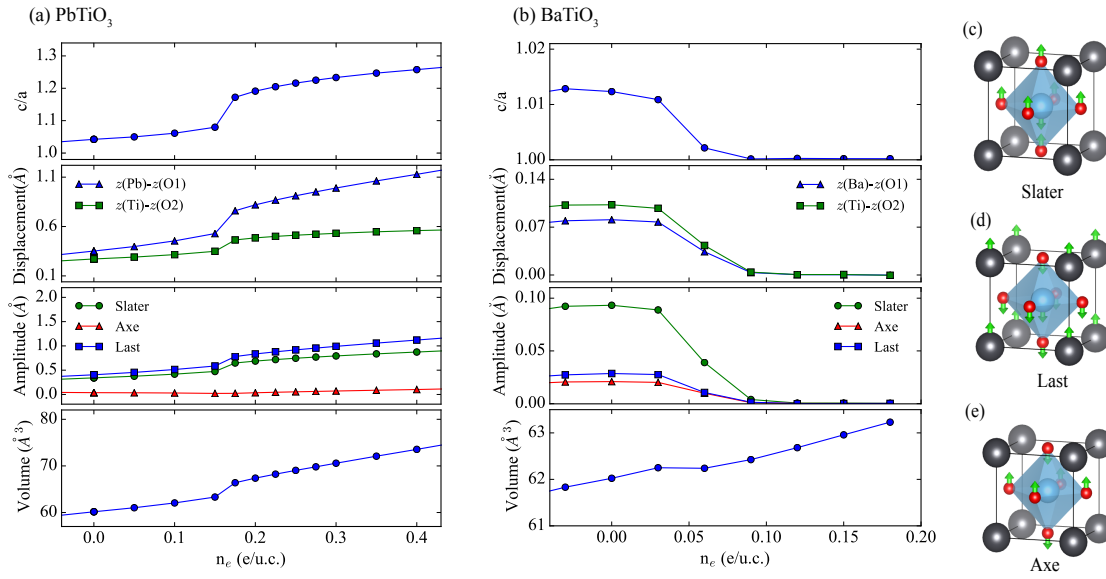


FIG. 2: The tetragonality (ratio of out-of-plane lattice constant c and the in-plane lattice constant a), the relative displacements of Pb-O ($z(\text{Pb}/\text{Ba}) - z(\text{O}1)$) and Ti-O ($z(\text{Ti}) - z(\text{O}2)$), the amplitudes of the polar modes, and the volume as functions of doped electron density n_e in (a) PbTiO_3 and BaTiO_3 are shown in (a) and (b), respectively. (c), (d), and (e) are the polar normal modes, namely the Slater, Axe, and Last modes.

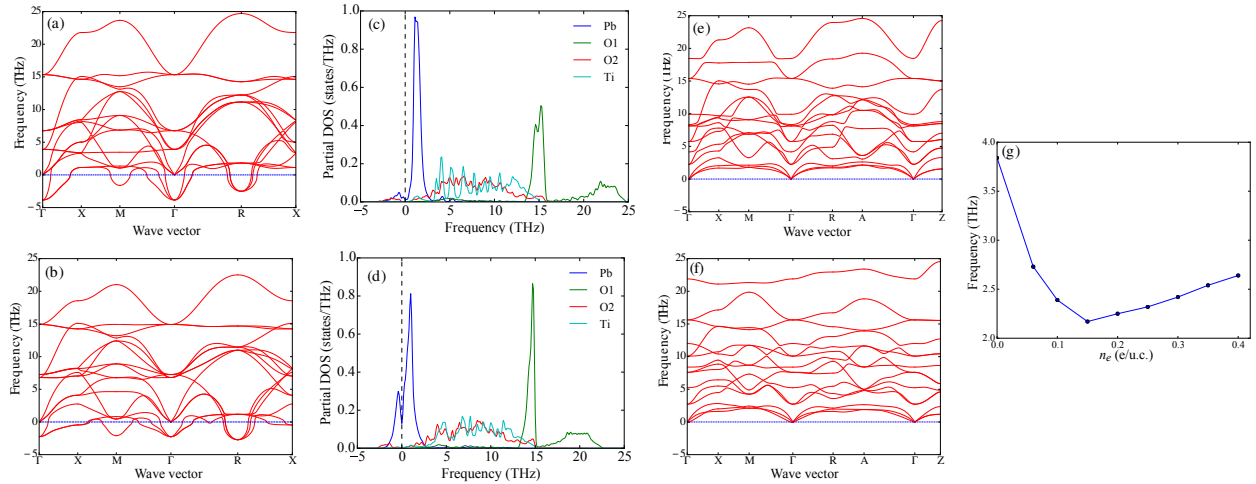


FIG. 3: The phonon band structures of the (a) $Pm\bar{3}m$ structure without doping, (b) $Pm\bar{3}m$ structure with electron doping ($n_e = 0.2$ e/u.c.), (e) $P4mm$ structure without doping, (f) $P4mm$ structure with electron doping ($n_e = 0.2$ e/u.c.). (c) and (d) are the atom projected partial phonon density of states projected on the $[001]$ direction for the $Pm\bar{3}m$ structure without doping and with electron doping ($n_e = 0.2$ e/u.c.), respectively. In (a), (b), (c), and (d), the imaginary phonon frequencies are shown as negative numbers. The high symmetry q-vectors for $Pm\bar{3}m$ are Γ (0, 0, 0), X (0, 1/2, 0), M (1/2, 1/2, 0), R (1/2, 1/2, 1/2). The high symmetry q-vectors for $P4mm$ are Γ (0, 0, 0), X (0, 1/2, 0), M (1/2, 1/2, 0), R (0, 1/2, 1/2), A (1/2, 1/2, 1/2), Z (0, 0, 1/2). (g) is the absolute values of the imaginary frequencies at Γ as a function of the electron doping levels.

and 4 type II Pb-O2 bonds. In PbTiO_3 and BaTiO_3 , the polar distortions are featured with the anti-parallel displacements of the cations (Pb, Ba, and Ti) and the anions (O), i.e. the positive values of cation-anion FC constants favor the polar distortion. In BaTiO_3 , the antiparallel displacement of Ti and O1 is favored because of the Ti $3d$ -O1 $2p$ hybridization, therefore the IFC is positive. As n_e increases, the Ti-O1 inter-atomic FC decreases. In PbTiO_3 , The Ti-O1 and Ti-O2 inter-atomic

FC also decreases. The decreasing of Ti-O IFC's and the increasing of the Ti self-force constants indicates that the Ti-site instability is reduced. The Pb-O and Ba-O IFC's increase with n_e in PbTiO_3 and BaTiO_3 . But only the Pb-O2 IFC is above zero, which drives the Pb ions away from their central symmetry positions. Whereas the Ba-O interaction cannot drive the polar distortion. The increasing of A-O FCs and the decreasing of the A-site self-force constants are the reasons for

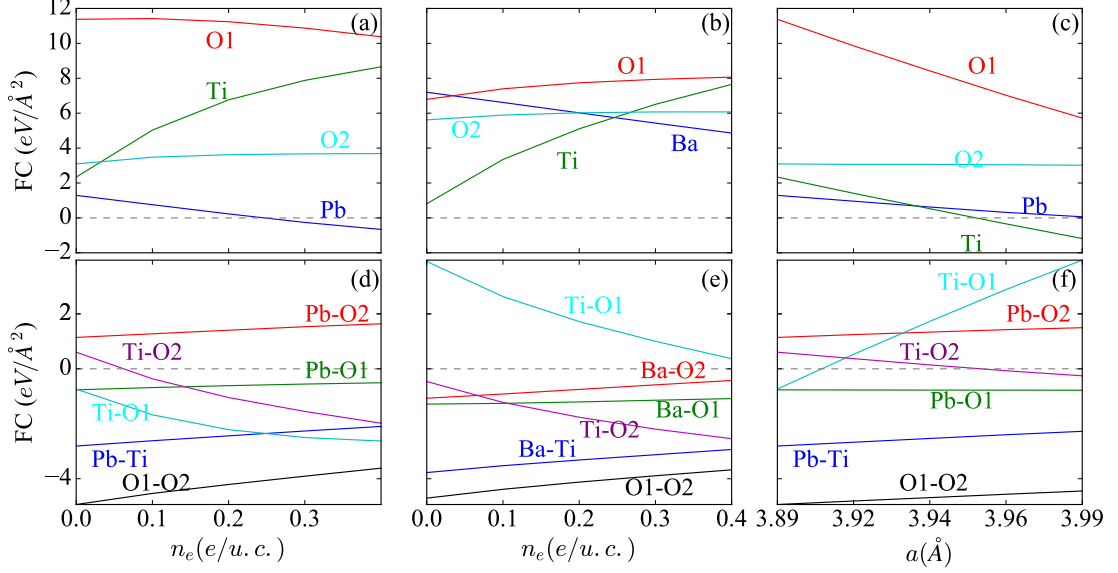


FIG. 4: Dependences of the FCM's on the concentration of doped electrons. (a) and (b) are the self-force constants on the different atoms in $Pm\bar{3}m$ $PbTiO_3$ and $BaTiO_3$, respectively. (d) and (e) are the IFC's between different pairs of atoms in $PbTiO_3$ and $BaTiO_3$, respectively. (c) and (f) are the self-force constants and the IFC's in the non-doped $Pm\bar{3}m$ $PbTiO_3$ structures, the lattice constants of which were fixed to these with electron doping. The lattice constants are corresponding to $n_{el} = 0.0-0.4$ e/u.c. .

increasing of the A-site instability.

Both the Ti-site Pb-site instabilities can be viewed as results of PJTE's which will be referred to as Ti PJTE and Pb PJTE in this work, respectively hereafter. To see why their responses to the electron doping are different, we calculated the electronic structure of $PbTiO_3$.

PJTE is through a mix of the ground state and the low excited states by vibronic coupling. Detailed descriptions of PJTE are in the works of Bersuker *et al.*²³⁻²⁵. In a high-symmetry $Pm\bar{3}m$ reference system, the energy E can be written as a function of a normal displacement q , where $\partial E/\partial q = 0$. If the curvature K of the energy E ,

$$K = (\partial^2 E/\partial q^2)_0 \quad (1)$$

is negative, the energy is at a local maximum, indicating that the system is unstable. E is the ground state eigenvalue of Hamiltonian H , ($E = \langle \psi_0 | H | \psi_0 \rangle$). K can be written in two parts,

$$K = K_0 + K_v \quad (2)$$

$$= \langle \psi_0 | (\partial^2 H/\partial q^2)_0 | \psi_0 \rangle + 2 \langle \psi_0 | (\partial H/\partial q)_0 | \psi'_0 \rangle$$

, in which, ψ_0 is the ground state, $\psi'_0 = (\partial \psi_0/\partial q)_0$.

Using the second order perturbation theory, we can get

$$K_v = -2 \sum_n \frac{|\langle \psi_0 | (\partial H/\partial q)_0 | \psi_n \rangle|^2}{E_n - E_0} \quad (3)$$

, in which ψ_n is an excited state; E_n and E_0 are the energies of the excited state and the ground state, respectively. It can be noticed that $K_v < 0$ if the mix of the ground state and the

excited state under the displacement q is allowed by symmetry. Thus K_v contributes to the instability. If the parity of the product of the ground state and the excited state is odd, the net overlap of them would be zero in the highest symmetry. However, with a polar vibration, the hybridization becomes non-zero, causing an energy gain. Therefore, the BJTE can be interpreted as added covalence in terms of bonding²⁶.

The instability of Ti atoms is due to the PJTE²³⁻²⁵. In the TiO_6 octahedron with Ti d^0 electronic configuration, the highest occupied states are the O $2p$ states, with configuration $(t_{1u} \downarrow)^3(t_{1u} \uparrow)^3$, and one electron transfer to the Ti $3d$ orbitals to form the lowest Excited states with configuration $(t_{1u} \downarrow)^3(t_{1u} \uparrow)^2(t_{2g} \uparrow)^1$. The net overlap of them would be canceled out if the Ti cation stays at the center of the octahedron; the polar mode vibration of the Ti cation would allow for an overlap and reduce the total energy, leading to a non-zero K_v , which is a driving force of the ferroelectricity. The “ d^0 ness” plays an essential role in this kind of PJTE. Electron doping pushes the Fermi energy into the bottom of the conduction band, which is mostly Ti $3d$ (Fig. 5 (a)), introducing d^1 electronic configuration, which has no PJTE⁵¹. For the d^1 configuration, the ground state would be $(t_{1u} \downarrow)^3(t_{1u} \uparrow)^3(t_{2g} \uparrow)^1$; and the lowest excited state would be $(t_{1u} \downarrow)^2(t_{1u} \uparrow)^3(t_{2g} \uparrow)^2$. The ground state and the excited state are of different spin multiplicity, therefore do not mix by the vibronic coupling. Thus, the Ti PJTE is suppressed as the electron doping increases.

The lone-pair mechanism of the ferroelectric materials with cations of s^2p^0 electronic configuration is another kind of PJTE^{52,53}. Regarding the Pb-O bonds, the electronic states near the Fermi-energy are the Pb $6s$ and $6p$ states, and the O $2p$ states. The occupied Pb $6s$ orbitals and the O $2p$ orbitals

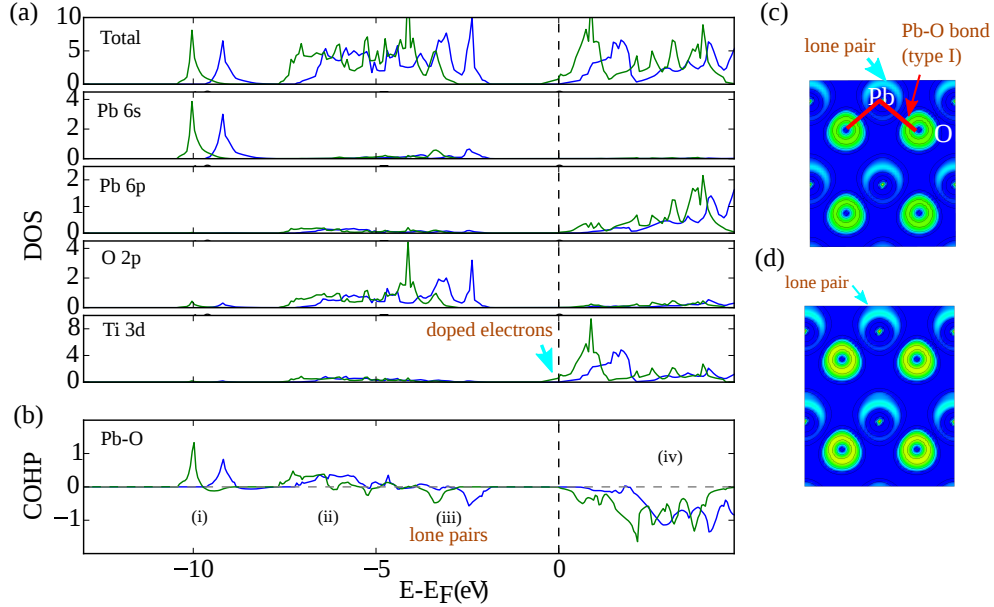


FIG. 5: (a) The density of states in PbTiO₃. (b) The COHP of the Pb-O bond. In (a) and (b), the blue lines and the green lines represent the results in the non-doped and doped PbTiO₃ structures, respectively. The results for non-doped structure are shifted so that the Fermi energy is at the conduction band minimum so that the DOSes for the doped and non-doped structures can be more easily compared. The concentration of the doped electrons is $n_e=0.2$ e/u.c.. (c) and (d) are the contour maps of the ELF in the $a - c$ PbO plane of the doped and non-doped structures, respectively.

form bonding states with energies of about -10 eV (region (i) in Fig. 5 (b)), and the anti-bonding states just below the Fermi energy (region (iii) in Fig. 5 (b)). These occupied (Pb 6s)-(O 2p) anti-bonding states can be seen as the ground states in equation (3); whereas the unoccupied Pb 6p states are the unoccupied excited states. The overlap of them has both positive and negative parts, which cancels out in the central symmetric cubic structure. However, the coupling between the ground and excited states becomes non-zero if Pb moves away from the central-symmetric position, which lowers the total energy and thus drives the polar distortion. The hybridization between the (Pb 6s-O 2p) bonding states with Pb 6p states results in bonding and antibonding states, corresponding to the region (ii) and region (iv), respectively. Therefore, the Pb PJTE effect can also be interpreted as added covalence²⁶ in the terms of bonding, which is believed to be the driving force for the Pb-site instability^{19,50}. The displacement of Pb reduces the type I Pb-O bond, leading to a strong covalency between Pb and O₂ ions. The hybridization also causes the asymmetric ELF lobes near at the Pb sites as shown in Fig. 5 (c) and (d), which is a characteristic of the lone-pair mechanism^{49,54}.

As can be seen from Fig. 5 (a) and (b), the unoccupied Pb 6p states, which are the excited states involved in the Pb PJTE, are above the Fermi energy when the electrons are doped. Therefore, the Pb PJTE will not be strongly affected by the electron doping. As a result, the change of the Pb self-force constant with electron doping is much smaller than that of Ti; the change of the Pb-O inter-atomic force constants are also much smaller than those of Ti-O, as shown in Fig. 4. There's no sig-

nificant reduction in the asymmetric lobe of the ELF in the doped structure (Fig. 5 (d)) than that in the non-doped structure (Fig. 5 (c)).

The increasing of the Pb site instability is likely to be the result of the increasing of the Pb-O distance with electron doping. The elongation of the Pb-O distance might cause a more under-bonded Pb which requires a larger displacement. The forces between the doped electrons on the Ti 3d bands and the negatively charged O anions are repulsive, which increases the Ti-O bond lengths and the Pb-O distances are also increased. Thus the overlap of the Pb and O orbitals decreases, which will lead to the decreasing of both $|K_0|$ and $|K_v|$. If $|K_0|$ decreases more slowly than $|K_v|$, the instability will increase, for example, Bersuker *et al.* showed that $|K_0|$ decreases more slowly than $|K_v|$ in the PJTE involving Ti-site in RTiO₃ (R=Ba, Sr, Ca). In terms of bonding, the PJTE can be interpreted as added covalent interaction. In perovskites, a tolerance factor t smaller (larger) than 1 implies an under-bonded A (B) site ion⁵⁵. The PJTE is effective when the added covalent interaction reduces the total energy, which tends to happen for an under-bonded ion. The increasing of B-site ion size decrease t , thus A-site ion becomes more under-bonded, which tends to enhance the PJTE. To test whether the enhancement of A-site instability is due to the increased Pb-O distance, we calculated the IFC's of PbTiO₃ without electron doping, and we fixed the lattice constants of the structures to those with electron doping. The results are in Fig. 4 (c) and (f). Indeed, the self-force constants of Pb, the IFC's of Pb-O1 and Pb-O2 in the non-doped structures are almost identical to those with electron doping,

which confirmed that the Pb-site instability is from increased Pb-O distance.

The self-force constant of Ti decreases, and the Ti-O1 IFC increases in the non-doped structure, just opposite to in the doped structures. This further shows that the increased occupation of the Ti $3d$ bands is the reason for the decreased Ti-site instability.

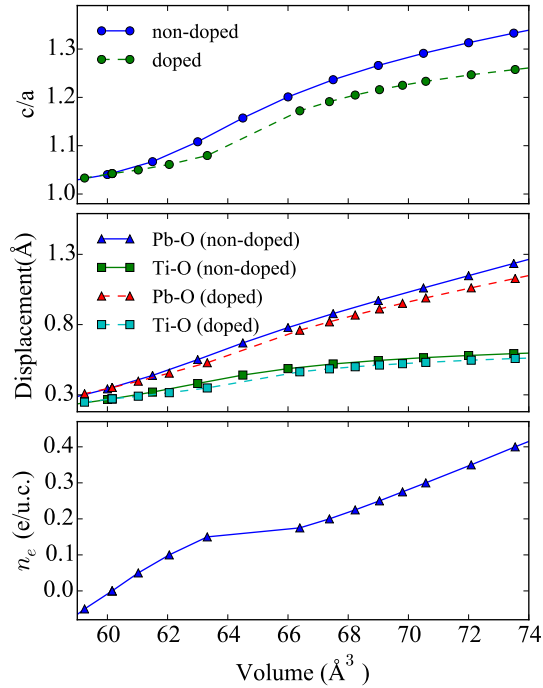


FIG. 6: (a) The ratio c/a as the function of lattice volume. (b) The relative displacements of Pb-O ($z(Pb) - z(O1)$) and Ti-O ($z(Ti) - z(O2)$) as functions of lattice volume. (c) The concentration of the doped electrons corresponding to the volume. The results for the non-doped structures were calculated by adding negative hydrostatic pressure.

We also noted that the change of the polar distortion with electron doping is very similar to that with the negative hydrostatic pressure in $PbTiO_3$. In both cases, the Pb-O bonds are stretched. We calculated the changes of the polar distortion of $PbTiO_3$ with negative hydrostatic pressure. The polar distortion increases with negative hydrostatic pressure in $PbTiO_3$, which agrees with previous studies⁵⁶⁻⁵⁸. The changes of the distortion with electron doping were plotted as functions of lattice volume and then compared to those with hydrostatic pressure, as shown in Fig. 6. The changes of c/a and cation-anion displacements with the same lattice volume are close in the two situations, indicating that the enhancement of the polar distortion might be from the same origin. It can be also seen that there is an anomalous enhancement of tetragonality and lattice volume as n_e increases to about 0.3 e/u.c. (Fig. 2), which was also found in $PbTiO_3$ with negative pressure⁵⁶. The polar distortions in the electron-doped structure are smaller than those in the non-doped structures with the same volume, which

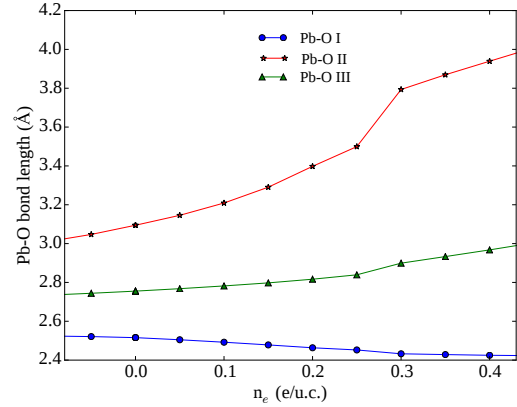


FIG. 7: The change of lengths the Pb-O bonds with the concentration of doped electrons.

may be the result of the screening effect.

It is interesting to note that the changes of polar distortion with negative hydrostatic pressure and that with electron doping are opposite in $BaTiO_3$, where the polar distortion also increases with the negative hydrostatic pressure^{56,57}, but decreases with the electron doping, though the volumes both increase in these two situations^{5,56,57}. The Ti-O bonds are stretched in the structure with negative hydrostatic pressure, therefore Ti becomes more under-bonded, which requires a larger polar distortion. Whereas in the electron-doped structure, the Ti-O short-range repulsion is enhanced due to the electrons on the Ti $3d$ bands and the suppression of Ti PJTE, leading to the reduced Ti-site instability. In both cases, the Ba-O bonds are stretched, leading to the enhanced Ba-O instability, which is however not enough to result in a polar distortion in electron-doped $BaTiO_3$. Consequently, the polar distortion in $BaTiO_3$ decreases with electron doping. It can be seen that the change of polar distortion in $BaTiO_3$ and $PbTiO_3$ can be uniformly viewed as the result of the decreased of A-site instability and increased B-site instability.

We examined the Pb-O bonds to see how the stretching of the Pb-O bonds affects the polar distortion. The lengths of the Pb-O bonds are plotted in Fig. 7. As the doped electrons enlarge the sizes of Ti ions and the lengths of Ti-O bonds, the Pb-O chain consisting of alternating type I and type II bonds are stretched. The changes of the type I bond lengths are relatively small, while those of the type II bond lengths are much larger. The reason is that the Pb-O electron hybridization stabilizes the short Pb-O type I bonds. And the enhanced Pb PJTE causes a larger displacement of Pb towards the side of type I bonds.

There are some similarities between the electron-doped $PbTiO_3$ and the NCSM $LiOsO_3$. Firstly, the A-site instability drives the polar distortion. Secondly, in both structures, the polar instabilities are due to the short-range interactions, which is the PJTE (or equivalently, the covalent interaction) for $PbTiO_3$, and short-range Coulomb interaction for $LiOsO_3$. Thirdly, the Fermi energy is in the B-site bands and outside the energy range of the electronic states related to the A-O in-

teraction. In LiOsO_3 , it was found that the ferroelectricity is due to the Li-O displacement, whereas the Fermi level lies in the Os bands⁹⁻¹². These similarities infer that the polar distortion caused by short-range interactions and the metallicity can coexist if they are from different atoms.

The mechanism of the persistent or even the enhancement of the polar distortion in PbTiO_3 with electron doping presented in this paper should be transferable to other lone-pair driven ferroelectric materials, like in PbVO_3 ⁵⁹, BiFeO_3 ^{60,61}, SnTiO_3 ⁴⁹, BiMnO_3 ⁵⁴. In these materials, the electronic states corresponding to the lone-pair mechanism are away from the Fermi energy if electrons are doped. Whereas the bottom of conduction bands in these materials are often the B-site states. Thus the doping of electrons can be seen as a selective enlargement of the B-site ion radius, which stretches the A-O bonds. Therefore, enhancement of polar distortion in these materials similar to that in PbTiO_3 is likely to emerge. These results also imply that the lone-pair stereoactive ions can be used as the A-site ions in perovskites to form NCSMs. By selecting a B-site element (or elements) with suitable ionic radius and itinerant electrons, lone-pair driven non-central-symmetric metal may be designed.

IV. CONCLUSION

In this work, we investigated the effect of electron doping on the lone-pair driven polar distortion by carrying out den-

sity functional theory studies on PbTiO_3 . We found that the polar distortion is enhanced with electron doping in PbTiO_3 even when the long-range Coulomb interaction is screened out by the doped electrons. The analysis on the phonons and electronic states show the mechanism for the persistent of the polar distortion: the lone-pair mechanism, which is the driving force of the polar distortion, is not strongly affected by the electron doping because the energy range of the related electron states is far enough from the Fermi energy. We also found that the enhancement of the polar distortion in PbTiO_3 is due to the increasing of the Ti ion radius, which caused the increasing of the Pb-O distance. These results show that the lone-pair driven polar distortion and the metallicity can coexist, and it is highly expected that the lone-pair stereoactive ions can be used in designing NCSMs.

ACKNOWLEDGMENTS

The work was supported by the National Basic Research Program of China (Nos. 2014CB921001 and 2012CB921403), the National Natural Science Foundation of China (No. 11134012), and the Strategic Priority Research Program (B) of the Chinese Academy of Sciences (No. XDB07030200).

-
- ¹ W. Cochran, *Advances in Physics* **9**, 387 (1960).
 - ² P. Ghosez, X. Gonze, and J.-P. Michenaud, *EPL (Europhysics Letters)* **33**, 713 (1996).
 - ³ L. Liu, H. Guo, H. Lu, S. Dai, B. Cheng, and Z. Chen, *J. Appl. Phys.* **97**, 054102 (2005).
 - ⁴ K. Page, T. Kolodiazhyi, T. Proffen, A. K. Cheetham, and R. Seshadri, *Phys. Rev. Lett.* **101**, 205502 (2008).
 - ⁵ Y. Wang, X. Liu, J. D. Burton, S. S. Jaswal, and E. Y. Tsymlal, *Phys. Rev. Lett.* **109**, 247601 (2012).
 - ⁶ Y. Iwazaki, T. Suzuki, Y. Mizuno, and S. Tsuneyuki, *Phys. Rev. B* **86**, 214103 (2012).
 - ⁷ P. W. Anderson and E. I. Blount, *Phys. Rev. Lett.* **14**, 217 (1965).
 - ⁸ Y. Shi, Y. Guo, X. Wang, A. J. Princep, D. Khalyavin, P. Manuel, Y. Michiue, A. Sato, K. Tsuda, S. Yu, *et al.*, *Nat. Mater.* **12**, 1024 (2013).
 - ⁹ H. Sim and B. G. Kim, *Phys. Rev. B* **89**, 201107 (2014).
 - ¹⁰ H. J. Xiang, *Phys. Rev. B* **90**, 094108 (2014).
 - ¹¹ G. Giovannetti and M. Capone, *Phys. Rev. B* **90**, 195113 (2014).
 - ¹² H. M. Liu, Y. P. Du, Y. L. Xie, J.-M. Liu, C.-G. Duan, and X. Wan, *Phys. Rev. B* **91**, 064104 (2015).
 - ¹³ D. Puggioni and J. M. Rondinelli, *Nat. Commun.* **5** (2014), 10.1038/ncomms4432.
 - ¹⁴ N. A. Benedek and T. Birol, *J. Mater. Chem. C* **4**, 4000 (2016).
 - ¹⁵ V. P. Mineev and Y. Yoshioka, *Phys. Rev. B* **81**, 094525 (2010).
 - ¹⁶ V. M. Edelstein, *Phys. Rev. B* **83**, 113109 (2011).
 - ¹⁷ V. M. Edelstein, *Phys. Rev. Lett.* **75**, 2004 (1995).
 - ¹⁸ V. M. Edelstein, *J. Phys.: Condens. Matter* **8**, 339 (1996).
 - ¹⁹ R. E. Cohen, *Nature* **358**, 136 (1992).
 - ²⁰ R. E. Cohen and H. Krakauer, *Ferroelectrics* **136**, 65 (1992).
 - ²¹ Y. Kuroiwa, S. Aoyagi, A. Sawada, J. Harada, E. Nishibori, M. Takata, and M. Sakata, *Phys. Rev. Lett.* **87**, 217601 (2001).
 - ²² H. Tanaka, Y. Kuroiwa, and M. Takata, *Phys. Rev. B* **74**, 172105 (2006).
 - ²³ I. Bersuker, *Physics Letters* **20**, 589 (1966).
 - ²⁴ I. B. Bersuker and B. G. Vekhter, *Ferroelectrics* **19**, 137 (1978).
 - ²⁵ I. Bersuker, *The Jahn-Teller Effect*: (Cambridge University Press, Cambridge, 2006).
 - ²⁶ I. B. Bersuker, *Chemical Reviews* **113**, 1351 (2013), pMID: 23301718.
 - ²⁷ G. Kresse and D. Joubert, *Phys. Rev. B* **59**, 1758 (1999).
 - ²⁸ G. Kresse and J. Furthmüller, *Phys. Rev. B* **54**, 11169 (1996).
 - ²⁹ J. P. Perdew and A. Zunger, *Phys. Rev. B* **23**, 5048 (1981).
 - ³⁰ G. Shirane, R. Pepinsky, and B. C. Frazer, *Acta Crystallogr.* **9**, 131 (1956).
 - ³¹ G. Sághi-Szabó, R. E. Cohen, and H. Krakauer, *Phys. Rev. Lett.* **80**, 4321 (1998).
 - ³² S. Baroni, S. de Gironcoli, A. Dal Corso, and P. Giannozzi, *Rev. Mod. Phys.* **73**, 515 (2001).
 - ³³ A. Togo and I. Tanaka, *Scr. Mater.* **108**, 1 (2015).
 - ³⁴ X. Gonze and C. Lee, *Phys. Rev. B* **55**, 10355 (1997).
 - ³⁵ R. M. Pick, M. H. Cohen, and R. M. Martin, *Phys. Rev. B* **1**, 910 (1970).
 - ³⁶ W. Zhong, R. D. King-Smith, and D. Vanderbilt, *Phys. Rev. Lett.* **72**, 3618 (1994).
 - ³⁷ Although DFPT is capable of calculating the dynamic matrix at arbitrary wave vector without using supercells, only the Γ -point result is outputted in the VASP implementation. Phonopy makes use of a larger supercell to calculate the phonon frequencies at a

- few other wave vectors and then make a Fourier interpolation to calculate the full phonon dispersion curve.
- ³⁸ R. Dronskowski and P. E. Bloechl, *J. Phys. Chem* **97**, 8617 (1993).
- ³⁹ V. L. Deringer, A. L. TchougrÃeff, and R. Dronskowski, *J. Phys. Chem. A* **115**, 5461 (2011), pMID: 21548594.
- ⁴⁰ S. Maintz, V. L. Deringer, A. L. TchougrÃeff, and R. Dronskowski, *J. Comput. Chem.* **34**, 2557 (2013).
- ⁴¹ J. Íñiguez, D. Vanderbilt, and L. Bellaiche, *Phys. Rev. B* **67**, 224107 (2003).
- ⁴² K. Momma and F. Izumi, *J. Appl. Crystallogr.* **41**, 653 (2008).
- ⁴³ J. H. Lee and K. M. Rabe, *Phys. Rev. B* **84**, 104440 (2011).
- ⁴⁴ J. C. Slater, *Phys. Rev.* **78**, 748 (1950).
- ⁴⁵ J. T. Last, *Phys. Rev.* **105**, 1740 (1957).
- ⁴⁶ J. D. Axe, *Phys. Rev.* **157**, 429 (1967).
- ⁴⁷ X. Wu, D. Vanderbilt, and D. R. Hamann, *Phys. Rev. B* **72**, 035105 (2005).
- ⁴⁸ H. Moriwake, C. A. J. Fisher, A. Kuwabara, and T. Hashimoto, *Japanese Journal of Applied Physics* **50**, 09NE02 (2011).
- ⁴⁹ K. C. Pitike, W. D. Parker, L. Louis, and S. M. Nakhmanson, *Phys. Rev. B* **91**, 035112 (2015).
- ⁵⁰ P. Ghosez, E. Cockayne, U. V. Waghmare, and K. M. Rabe, *Phys. Rev. B* **60**, 836 (1999).
- ⁵¹ I. B. Bersuker, *Phys. Rev. Lett.* **108**, 137202 (2012).
- ⁵² I. B. Bersuker, *Ferroelectrics* **164**, 75 (1995).
- ⁵³ A. Walsh, D. J. Payne, R. G. Egdell, and G. W. Watson, *Chem. Soc. Rev.* **40**, 4455 (2011).
- ⁵⁴ R. Seshadri and N. A. Hill, *Chem. Mater.* **13**, 2892 (2001).
- ⁵⁵ M. Ghita, M. Fornari, D. J. Singh, and S. V. Halilov, *Phys. Rev. B* **72**, 054114 (2005).
- ⁵⁶ S. Tinte, K. M. Rabe, and D. Vanderbilt, *Phys. Rev. B* **68**, 144105 (2003).
- ⁵⁷ H. Moriwake, Y. Koyama, K. Matsunaga, T. Hirayama, and I. Tanaka, *Journal of Physics: Condensed Matter* **20**, 345207 (2008).
- ⁵⁸ J. Wang, B. Wylie-van Eerd, T. Sluka, C. Sandu, M. Cantoni, X.-K. Wei, A. Kvasov, L. J. McGilly, P. Gemeiner, B. Dkhil, *et al.*, *Nat. Mater.* **14**, 985 (2015).
- ⁵⁹ D. J. Singh, *Phys. Rev. B* **73**, 094102 (2006).
- ⁶⁰ P. Ravindran, R. Vidya, A. Kjekshus, H. Fjellvåg, and O. Eriksson, *Phys. Rev. B* **74**, 224412 (2006).
- ⁶¹ X. He, K. J. Jin, H. Z. Guo, and C. Ge, *Phys. Rev. B* **93**, 174110 (2016).